

Defect healing and charge transfer mediated valley polarization in $\text{MoS}_2/\text{MoSe}_2/\text{MoS}_2$ trilayer van der Waals heterostructures

Alessandro Surrente,[†] Dumitru Dumcenco,[‡] Zhuo Yang,[†] Agnieszka Kuc,[¶] Yu
Jing,[¶] Thomas Heine,[¶] Yen-Cheng Kung,[‡] Duncan K. Maude,[†] Andras Kis,[‡] and
Paulina Plochocka^{*,†}

[†]*Laboratoire National des Champs Magnétiques Intenses, UPR 3228,
CNRS-UGA-UPS-INSA, Grenoble and Toulouse, France*

[‡]*Electrical Engineering Institute and Institute of Materials Science and Engineering, École
Polytechnique Fédérale de Lausanne, CH-1015 Lausanne, Switzerland*

[¶]*University of Leipzig, Wilhelm Ostwald Institute of Physical and Theoretical Chemistry
Leipzig, Saxony, Germany*

[§]*School of Engineering and Science, Jacobs University Bremen, Campus Ring 1, 28759
Bremen, Germany*

E-mail: paulina.plochocka@lncmi.cnrs.fr

Abstract

Monolayer transition metal dichalcogenides (TMDC) grown by chemical vapor deposition (CVD) are plagued by a significantly lower optical quality compared to exfoliated TMDC. In this work we show that the optical quality of CVD-grown MoSe_2 is completely recovered if the material is sandwiched in $\text{MoS}_2/\text{MoSe}_2/\text{MoS}_2$ trilayer van der Waals heterostructures. We show by means of density-functional theory that this

remarkable and unexpected result is due to defect healing: S atoms of the more reactive MoS₂ layers are donated to heal Se vacancy defects in the middle MoSe₂ layer. In addition, the trilayer structure exhibits a considerable charge-transfer mediated valley polarization of MoSe₂ without the need for resonant excitation. Our fabrication approach, relying solely on simple flake transfer technique, paves the way for the scalable production of large-area TMDC materials with excellent optical quality.

Keywords

Chemical Vapor Deposition, transition metal dichalcogenides, van der Waals heterostructures, defect healing, charge transfer mediated valley polarization

Monolayer transition metal dichalcogenides (TMDC) have a direct bandgap situated in the visible range, which makes them ideal building blocks for novel electronic and optoelectronic devices.¹⁻¹⁰ The bandgap of monolayer TMDCs occurs at the inequivalent (but degenerate) K and K' points of the hexagonal Brillouin zone. The broken inversion symmetry of a TMDC monolayer combined with the time reversal symmetry imposes opposite magnetic moments at the K and K' valleys. This in turn determines the characteristic circular dichroism exhibited by these materials, wherein each valley can be addressed separately with circularly polarized light of a given helicity.¹¹⁻¹³ Additionally, optical spectra are influenced by the strong spin-orbit coupling, which lifts the degeneracy of band states at the valence band edges, resulting in well-resolved A and B resonances, as observed in reflectivity or absorption spectra.^{2,14-16} The interplay of spin-orbit coupling with broken inversion symmetry and time reversal symmetry locks the valley and spin degrees of freedom, making TMDC attractive candidates for valleytronics.¹⁷ The spin-valley index locking along with the large

distance in the momentum space between K and K' valleys preserves the valley polarization observed in the degree of circular polarization (DCP) in helicity resolved photoluminescence emission.¹⁸⁻²²

Applications require a scalable fabrication platform providing high-quality large-area monolayer TMDC. Unfortunately, the most promising approach today, namely chemical vapor deposition (CVD) growth²³⁻²⁷ struggles to compete with exfoliated TMDC in terms of sample quality. Low temperature PL spectroscopy of CVD-grown MoS₂ and MoSe₂ reveals broad emission from defect bound excitons, which is significantly more intense than the free exciton peak²⁸⁻³⁰ and is related to chalcogen vacancies induced during the CVD growth.^{29,30}

Here, we demonstrate a novel approach to neutralize the intrinsic defects of CVD-grown TMDCs, using flake transfer tools routinely employed in the fabrication of van der Waals heterostructures.³¹⁻³³ We investigate the optical properties of trilayer stacks composed of external CVD-grown MoS₂ flakes²⁴ as capping layers and an internal CVD-grown MoSe₂ flake which has a smaller bandgap.^{34,35} Remarkably, this fabrication approach strongly suppresses the localized exciton emission in MoSe₂, yielding a low temperature PL comparable to that observed in mechanically exfoliated samples. This striking result can be understood from density functional theory (DFT), which suggests that the more reactive MoS₂ donates chalcogen atoms to heal vacancy defects in MoSe₂. Incorporating MoS₂ into the trilayer heterostructure furthermore allows us to demonstrate a new way to introduce valley polarization in MoSe₂. Due to the type II band alignment in TMDC heterojunctions,³⁵ a significant charge transfer is observed in these systems.^{32,36,37} Our results show that spin of the hole is conserved upon charge transfer from MoS₂ to MoSe₂ after excitation in resonance with MoS₂ A exciton. This leads to non-zero steady state valley polarization in MoSe₂, which has never been observed before under non-resonant excitation.³⁸⁻⁴⁰

Defect healing

The sample with MoS₂/MoSe₂/MoS₂ trilayer stacks and micrograph of a representative transfer area are schematically shown in Fig. 1(a) and (b). Low temperature microPL (μ PL) spectroscopy has been used to characterize *as-grown* CVD samples on the sapphire substrate (prior to any transfer process) and the trilayer MoS₂/MoSe₂/MoS₂ stack. All spectra shown in Fig. 1(c) and (d) were measured under nominally identical conditions with an excitation power of 100 μ W (see Fig. S1 in Supporting Information (SI) for power dependent μ PL spectra). The *as-grown* MoS₂ and MoSe₂ monolayers both show a broad PL feature (full width at half maximum, FWHM, of 258 meV and 106 meV, respectively) related to emission from excitons bound to defect or charge impurity states.^{28–30,41} A-exciton emission (labeled X_A in Fig. 1(c)) is seen only as a weak peak or shoulder at higher energies. These assignments are confirmed by reflectivity contrast measured on the same spot. Reflectivity contrast is defined as $\Delta R/R_s = (R - R_s)/R_s$, where R is the reflectivity spectrum measured on the sample and R_s denotes the reflectivity spectrum measured on the substrate. In the case of transparent substrates such as sapphire, reflectivity contrast is proportional to the absorption of the sample.⁴² The reflectivity contrast spectrum of as-grown MoS₂ (see upper panel of Fig. 1(c)) consists of a main peak at 1.937 eV and a higher energy, weaker feature at 2.085 eV, related to the spin-orbit split B exciton. The energy difference of 148 meV corresponds very well to theoretically predicted spin-orbit splitting of the valence band⁴³ and is very similar to the splitting determined with transmission measurements on similar samples.³⁴ The reflectivity contrast spectrum of as grown MoSe₂, shown in the central panel of Fig. 1(c) has a peak at 1.637 eV, which corresponds well to the high energy shoulder of the μ PL spectrum and hence is assigned to A exciton. As in our previous study,³⁴ we are unable to resolve the B exciton in reflectivity contrast measurements on as grown MoSe₂.

The optical properties of the trilayer stack are dramatically improved (bottommost panel in Fig. 1(c)). The most striking difference is the nearly total suppression of (i) emission from defect bound excitons, and (ii) significant quenching of both MoS₂ PL, barely seen as a weak

peak at 1.929 eV, and of MoSe₂ PL (overall integrated intensity decrease by two and one orders of magnitude, respectively, see Fig. S2 in SI). The measured PL spectrum is dominated by narrow free neutral (X_A) and charged exciton (T) emission in MoSe₂ (low power FWHM of 11 meV and 10 meV, respectively, see Fig. S1 in SI), approaching the quality of exfoliated WSe₂ embedded in boron nitride (FWHM \sim 10 meV).⁴⁴ The free exciton emission overlaps with a weak broad background emission from the sapphire substrate (the narrow peak just below 1.8 eV corresponds to the emission from a color center in sapphire). The highest energy peak in the reflectivity contrast spectrum of the trilayer (see Fig. 1(c), bottom panel), blue shifted with respect to the A exciton peak of MoS₂ by 145 meV is attributed to the B exciton of MoS₂. The peak related to MoS₂ A exciton in the reflectivity contrast spectrum is blue shifted by 27 meV with respect to the corresponding PL peak. This Stokes shift has been attributed to the presence of a high doping level in MoS₂,¹⁶ also present in our layers.⁴⁵ On the low energy side of the μ PL spectrum, the two distinct peaks at 1.674 eV and 1.645 eV are assigned to the A exciton and to the trion of MoSe₂, respectively. The trion binding energy of 29 meV is very similar to that reported in other studies on MoSe₂.^{29,46}

The high optical quality of the MoSe₂ embedded in the heterostructure enabled us to resolve an additional peak at 1.87 eV in the reflectivity contrast spectrum, assigned to the B exciton of MoSe₂.^{43,47} The vastly improved optical properties suggest a defect healing process, in which the contact with MoS₂ is enough to drastically reduce the number of defects in MoSe₂. The quenching of the intralayer emission^{32,37} in the trilayer is manifestation of a fast charge transfer mechanism^{36,48} related to the type II band alignment in MoS₂/MoSe₂ heterostructures.³⁵ The weak luminescence of MoS₂ is consistent with a background n doping⁴⁵ of the as grown layers and with an additional charge transfer after the formation of the heterostructure. We assign the brighter emission from MoSe₂ (in the trilayer) to the hole transfer to an intrinsically n doped material and to the defect healing effect, combined with luminescence resulting from higher energy states, similar to hot luminescence of direct exciton in multilayer MoSe₂.^{49,50} The long range optical uniformity of the trilayer stacks

has been monitored by acquiring PL with a gradually defocused excitation beam. The acquired PL spectra are displayed in Fig. 1(d). For an excitation spot size of 10 μm , the defect emission remains strongly suppressed. For larger spot sizes, a broad low-energy peak starts to emerge, probably due to defect related emission in MoSe_2 in areas which are not fully capped. These measurements are a proof of concept, demonstrating that this approach, when optimized, should enable the fabrication of large area CVD-grown heterostructures with excellent optical quality.

Previous attempts at improving the optical properties of CVD-grown MoSe_2 using HBr treatment²⁹ or the isoelectronic impurity substitution³⁰ have met with only partial success: Impurity-bound excitons still remained the most prominent component of the emission spectrum. Low temperature PL spectra consisted in broad features, wherein free exciton emission could be identified only after fitting. The optical properties of exfoliated MoS_2 have been improved by superacid treatment.⁵¹ In our case, the simple act of bringing MoSe_2 in intimate physical contact with MoS_2 , a procedure that can be performed after growth and does not require any chemical functionalisation, results in a virtually complete suppression of emission from the impurity-bound states and a spectrum in which the trion and exciton resonances can be clearly resolved.

Our defect healing hypothesis is further supported by the results obtained from DFT simulations. We have calculated the gain of energy in a heterobilayer $\text{MoSe}_2/\text{MoS}_2$ using two models: A single Se vacancy in the MoSe_2 layer (Model 1) and a single S vacancy in the MoS_2 layer together with a single S substitution in the MoSe_2 layer (Model 2). This corresponds to the transfer energy of a S atom from pristine MoS_2 to heal a defect in MoSe_2 . We observe a significant energy gain of 18 kJ mol^{-1} (180 meV) per S transfer from MoS_2 to the MoSe_2 defect, which shows that defect healing in MoSe_2 by MoS_2 is thermodynamically favored. The formation energy of a S vacancy in a MoS_2 monolayer has been theoretically estimated in the 1.3 eV–1.5 eV range.^{52,53} We consider these as upper bounds for the energy barrier of the transfer of a S atom to fill a Se vacancy in MoSe_2 , because this is not a static

process but a transfer between two neighbouring layers.

We have also calculated the band structures of a perfect MoSe₂ monolayer, MoSe₂ monolayer with one Se vacancy, and MoSe₂ monolayer with one Se→S substitution. We observe that Se vacancies introduce strongly localized states in the bandgap of MoSe₂, 0.92 eV above the top of the valence band (see Fig. 2). These are dispersionless and act as trap centers. Healing the Se vacancy with S substitution restores the band structure of a nearly perfect MoSe₂ monolayer. In the studied 5 × 5 supercell model (2% Se→S substitutions), the bandgap increases by only 1 meV.

Charge transfer mediated valley polarization

First signatures of charge transfer between the layers are seen in the comparison between PL intensities of as grown layers and trilayers, shown in Fig. S2 of SI. Additional insights is provided by the spatial correlation of the PL intensity of the MoS₂ and MoSe₂. The integrated spatial map of the MoSe₂ A exciton is shown in Fig. 3(a). The signal is particularly intense at positions where the overlap between the three layers is good and the material does not have a large number of defects. This implies that the bright spots do not necessarily have a triangular shape. This map provides an additional opportunity to demonstrate the high degree of uniformity of the emission of MoSe₂ incorporated in a heterostructure, by extract μ PL spectra. We show in Fig. 3(b) five μ PL spectra measured at 10 μ m distance from one another. The spectra have been normalized by the integration time. We note that emission from defect states is consistently absent in the five spectra and the similar line shape points to a good uniformity of the emission over the full mapped area. In Fig. 3(c), we overlay the intensity map of MoS₂ with that of MoSe₂, forcing the areas having the lowest signal from the latter to be transparent. These areas correspond to zones where the signal from MoS₂ is highest. We quantify the observed intensity (anti)correlation by plotting in Fig. 3(d) the ratio between the intensity of A exciton in one material normalized by the total emission of both

materials [$I_{\text{Mo}X_2}/(I_{\text{MoS}_2} + I_{\text{MoSe}_2})$, where $X = \text{S}$ or Se]. It can be noted that when the emission of MoSe_2 becomes more pronounced, the emission of MoS_2 decreases correspondingly. This is fully consistent with charge transfer. In positions where the three layers overlap efficiently, charge transfer induces a quenching of the MoS_2 PL. At the same time, the PL from MoSe_2 is particularly intense at these positions owing to efficient defect healing, but still weaker than in as grown MoSe_2 samples (see Fig. S2 in SI).

Photoluminescence excitation (PLE) spectroscopy is a useful tool to investigate more thoroughly the charge transfer processes. We focus our measurements on MoSe_2 incorporated in a trilayer stack. In Fig. 4(a), we show the PLE measured without making use of polarization optics. Both PLEs of the A exciton and trion have been normalized by the weakest intensity measured at an excitation energy of 1.999 eV in order to be able to compare the enhancement effects for the exciton and trion. The integrated intensities of both peaks show a pronounced maximum when the excitation energy is close to the resonance with the B exciton of MoSe_2 .⁵⁴ The integrated intensity is consistently lower than this maximum at other excitation energies, including those corresponding to resonances in MoS_2 (see for example the weak peak corresponding to MoS_2 X_A , appearing as a shoulder of the main PLE peak in Fig. 4(a)). This is the exact opposite of what is observed in a heterostructure system where energy transfer has been demonstrated. In such system, the emission intensity of one material is significantly enhanced when the excitation energy is resonant with excitonic transitions of the other material.⁵⁵ This consideration allows us to safely rule out energy transfer between the different layers.

To investigate whether the trilayer stack shows charge transfer, we initially consider the normalized intensity of exciton and trion when the excitation energy is resonant with excitonic transitions of MoS_2 . For resonances with both A and B exciton of MoS_2 , the emission intensity is enhanced more for MoSe_2 A exciton than for the trion. This is consistent with the presence of a large n-type background doping (free electrons) in CVD-grown MoSe_2 , which gives rise to strong charged exciton emission even in the absence of gating (see Fig. 1(a)).

For a MoS₂/MoSe₂ heterojunction, the band alignment promotes the transfer of holes from MoS₂ to MoSe₂.³⁵ When we optically excite the trilayer stack, we induce a net transfer of holes from MoS₂ to MoSe₂, resulting in a relatively stronger emission of the neutral exciton as compared to the trion.⁵⁵

We also performed circular polarization resolved PLE focusing on MoSe₂ incorporated in a trilayer stack. When the excitation energy is far from resonance (A or B excitons of both materials), MoSe₂ shows an extremely small valley polarization. This is illustrated by the polarization-resolved μ PL spectra of Fig. 4(b), where a negligibly small DCP, defined as $DCP = [I_{\sigma_1} - I_{\sigma_2}] / [I_{\sigma_1} + I_{\sigma_2}]$, is observed across the entire energy range of interest.³⁸ When the excitation energy of the laser was tuned to the proximity of the resonance with the A exciton of MoS₂, a significant valley polarization accumulates. An example of polarization resolved spectra at an excitation energy resonant with A exciton of MoS₂ is shown in Fig. 4(c). The valley polarization is quantified by a slightly positive DCP at energies around A exciton and trion of MoSe₂ (see Fig. 4(c)). In Fig. 4(d) we illustrate the excitation energy dependence of the integrated DCP (estimated by extracting the relevant integrated intensity of exciton and trion with Gaussian fits). We notice a significant increase of the integrated DCP at energies corresponding to the A exciton resonance of MoS₂ (see dashed line in Fig. 4(d)), with a low energy shoulder possibly related to an enhanced DCP at excitation energies corresponding to MoSe₂ B exciton.³⁸ Polarization resolved electroluminescence of single and multilayer MoSe₂⁵⁶ as well as polarization resolved PL of indirect excitons emitted by a WSe₂/MoSe₂ heterostructure⁵⁷ have demonstrated higher degree of circular polarization. However, the mechanisms leading to polarized emission in these systems are fundamentally different from those yielding polarized PL of MoSe₂,⁵⁶ which is virtually impossible to achieve unless the PL is excited using quasi-resonant excitation in X_A of MoSe₂.³⁸⁻⁴⁰

We ascribe the observed MoSe₂ valley polarization to the hole transfer from MoS₂, with a mechanism schematically illustrated in Fig. 4(e). We excite the trilayer stack with circularly polarized light with a given helicity and in resonance with the A exciton of MoS₂. The

valley polarization directly created in MoSe₂ is quickly lost, which results in a negligible DCP, similarly to non-resonant excitation (see Fig. 4(d)). Resonant excitation in MoS₂ creates valley polarization for a duration estimated in the hundreds of femtoseconds range.⁵⁸ Charge transfer in van der Waals heterostructures is an ultra fast process, with upper bounds in the tens of femtoseconds range (hole transfer from MoS₂ has been reported to be faster than 50 fs³⁶). During this very rapid transfer, we assume that the hole spin (and thus valley due to the large spin orbit splitting in the valence band) is conserved, and, owing to the excess electron population in the MoSe₂ layer, the injected hole forms an exciton populating the valley corresponding to the helicity of the incoming light. These excitons have presumably a low kinetic energy (no excess energy of the photocreated hole), which slows down significantly the inter-valley scattering rate due to electron-hole exchange interaction.⁵⁹ As a result, this hole transfer is responsible for the observed valley polarization.

Conclusions

A detailed investigation of the optical properties of MoS₂/MoSe₂/MoS₂ trilayers reveals that stacking dramatically improves the optical quality of CVD-grown MoSe₂, essentially eliminating all defect bound exciton and MoS₂-related emission. These results open the way to using CVD-grown TMDCs for applications and studies that require materials with excellent optical quality. Photoluminescence spectra from MoSe₂ in a trilayer stack are dominated by narrow neutral and charged A exciton emission, resembling the spectrum of a high quality mechanically exfoliated flake. Density functional calculations confirm a defect healing scenario in which S atoms replace Se vacancies. Circular polarization resolved PL measurements demonstrate that MoSe₂ exhibits a significant valley polarization even when the excitation energy is far from the A exciton resonance. This behavior is the signature of an efficient spin-conserving hole transfer from MoS₂ to MoSe₂. Our approach provides a robust and straightforward method of healing defects in CVD-grown samples, which might

also be beneficial for the transport properties of these materials.

Acknowledgments

This work was partially supported by ANR JCJC project milliPICS, the Région Midi-Pyrénées under contract MESR 13053031, BLAPHENE project under IDEX program Emergence, “Programme des Investissements d’Avenir” under the program ANR-11-IDEX-0002-02, reference ANR-10-LABX-0037-NEXT, Swiss SNF Sinergia Grant no. 147607, the European Commission (ITN MoWSeS, GA 317451), and Deutsche Forschungsgemeinschaft (HE 3543/27-1 and GRK 2247/1 (QM3)). Y.J., A.K. and T.H. thank ZIH Dresden for super-computer time. This project has received funding from the European Union’s Horizon 2020 research and innovation programme under grant agreement No. 696656 (Graphene Flagship).

Supporting Information Available

The following files are available free of charge.

Supporting information: Low temperature μ PL spectra, comparison of μ PL spectra of as-grown versus trilayer samples, temperature dependent μ PL spectra and time-resolved PL.

Methods

Sample preparation

The sample with $\text{MoS}_2/\text{MoSe}_2/\text{MoS}_2$ trilayer stacks, schematically shown in Fig. 1(a), was obtained by two separate transfer steps using a wet transfer KOH method.³² First of all, the upper- MoS_2 was transferred onto the as-grown MoSe_2 monolayer on sapphire.^{24,34} Subsequently, the $\text{MoS}_2/\text{MoSe}_2$ stack was transferred onto an as-grown bottom MoS_2 monolayer on sapphire. For both transfers, sapphire chips with material (upper- MoS_2 or $\text{MoS}_2/\text{MoSe}_2$

stack) were first spin coated with PMMA 950 at 1500 rpm for 60 s and baked at 180 °C for 5 minutes. The films were detached in KOH (30%) at moderate temperatures (70 °C), washed 3 times in deionized water, transferred onto sapphire with the stacking layer (MoSe₂ or bottom-MoS₂) and dried at 50 °C for 30 minutes. The PMMA was removed by dipping the sample in acetone for 12 hours, followed by rinsing with isopropanol and drying in a N₂ flow. Such method provides a polymer clean interface of stacks and minimal damage of material caused by the transfer process. Using this method, a large area film with monolayer (MoS₂), bilayer (MoSe₂/MoS₂, MoS₂/MoS₂ and MoS₂/MoSe₂ stacks) and trilayer (MoS₂/MoSe₂/MoS₂ stack) was obtained. A micrograph of a representative transfer area is shown in Fig. 1(b). To determine the position of areas with different number of stacked layers, Ni markers were deposited.

Optical measurements

For the optical characterization, the sapphire substrate was mounted on the cold finger of a He-flow cryostat. The excitation was provided either by a CW frequency doubled solid state laser emitting at 532 nm or by the frequency doubled output of an optical parametric oscillator (OPO), synchronously pumped by a mode-locked Ti:sapphire laser. The typical temporal pulse width was 300 fs, with a repetition rate of 80 MHz. The excitation beam was focused on the sample by a 50× microscope objective, giving a spot size of approximately 1 μm and having a numerical aperture of 0.55. The emitted PL was collected through the same objective and redirected to a spectrometer equipped with a liquid nitrogen cooled CCD camera or (for time-resolved measurements) to an imaging spectrometer and detected using a synchroscan streak camera with the temporal resolution set to 5 ps. All the spectra have been measured at 5 K, unless otherwise specified.

For spatial mapping the emission has been monitored while the optical cryostat was displaced with respect to the microscope objective using high precision motorized $x - y$ translation stages (1 μm step). The integrated intensity of given features (*e.g.* A exciton

emission) has been obtained by performing Gaussian fitting of the measured μ PL spectra.

Density functional theory of band structure in MoSe₂/MoS₂ heterobilayers

We have calculated heterobilayers made of MoSe₂ and MoS₂ monolayers, using DFT as implemented in the Crystal09 software.⁶⁰ We employed all-electron Gaussian-type bases of triple-quality,^{61,62} while Mo atoms were treated with the HAYWSC-311(d31)G basis with effective core potential set,⁶³ together with the PBE gradient corrected density functional.⁶⁴ London-dispersion interactions were accounted for using the approach proposed by Grimme (DFT-D3).⁶⁵ Full optimization of atomic positions and lattice vectors was performed on both models: Model 1 with perfect MoS₂ monolayer and one Se vacancy in the MoSe₂ monolayer, and Model 2 with one S vacancy in the MoS₂ monolayer and one S substitution in the MoSe₂ monolayer. The models are built of 5×5 supercells (see Fig. 2).

Geometry optimization only slightly alters the lattice geometry (see Table 1).

Table 1: Structural parameters of MoS₂/MoSe₂ defective heterostructures giving the lattice constant (a) and interlayer metal-to-metal distances (d).

System	a (Å)	d (Å)
MoS ₂ 1L	3.171	-
MoSe ₂ 1L	3.251	-
MoS ₂ /MoSe ₂	3.214	6.21
Model 1	3.206	6.30
Model 2	3.203	6.26

For the large supercells, which still overestimate the defect density in experiment, the defects studied here do not introduce any drastic changes into the structural properties of the systems. However, we note that we are constrained with the commensurate models of a heterobilayer, in which the corresponding monolayers are slightly distorted compared with the relaxed monolayers 3.251 Å and 3.171 Å for MoSe₂ and MoS₂, respectively. For a perfect

heterobilayer (3.214 Å), this gives 1.15% compression of MoSe₂ and 1.4% elongation of MoS₂.

References

- (1) Splendiani, A.; Sun, L.; Zhang, Y.; Li, T.; Kim, J.; Chim, C.-Y.; Galli, G.; Wang, F. *Nano Letters* **2010**, *10*, 1271–1275.
- (2) Mak, K. F.; Lee, C.; Hone, J.; Shan, J.; Heinz, T. F. *Physical Review Letters* **2010**, *105*, 136805.
- (3) Radisavljevic, B.; Radenovic, A.; Brivio, J.; Giacometti, V.; Kis, A. *Nature Nanotechnology* **2011**, *6*, 147–150.
- (4) Kuc, A.; Zibouche, N.; Heine, T. *Physical Review B* **2011**, *83*, 245213.
- (5) Lopez-Sanchez, O.; Lembke, D.; Kayci, M.; Radenovic, A.; Kis, A. *Nature Nanotechnology* **2013**, *8*, 497–501.
- (6) Baugher, B. W.; Churchill, H. O.; Yang, Y.; Jarillo-Herrero, P. *Nature Nanotechnology* **2014**, *9*, 262–267.
- (7) Ross, J. S.; Klement, P.; Jones, A. M.; Ghimire, N. J.; Yan, J.; Mandrus, G.; Taniguchi, T.; Watanabe, K.; Kitamura, K.; Yao, W.; Cobden, D. H.; Xu, X. *Nature Nanotechnology* **2014**, *9*, 268–272.
- (8) Pospischil, A.; Furchi, M. M.; Mueller, T. *Nature Nanotechnology* **2014**, *9*, 257–261.
- (9) Koppens, F. H. L.; Mueller, T.; Avouris, P.; Ferrari, A. C.; Vitiello, M. S.; Polini, M. *Nature Nanotechnology* **2014**, *9*, 780–793.
- (10) Mak, K. F.; Shan, J. *Nature Photonics* **2016**, *10*, 216–226.
- (11) Cao, T.; Wang, G.; Han, W.; Ye, H.; Zhu, C.; Shi, J.; Niu, Q.; Tan, P.; Wang, E.; Liu, B.; Ji, F. *Nature Communications* **2012**, *3*, 887.

- (12) Zeng, H.; Dai, J.; Yao, W.; Xiao, D.; Cui, X. *Nature Nanotechnology* **2012**, *7*, 490–493.
- (13) Mak, K. F.; He, K.; Shan, J.; Heinz, T. F. *Nature Nanotechnology* **2012**, *7*, 494–498.
- (14) Li, Y.; Chernikov, A.; Zhang, X.; Rigosi, A.; Hill, H. M.; van der Zande, A. M.; Chenet, D. A.; Shih, E.-M.; Hone, J.; Heinz, T. F. *Physical Review B* **2014**, *90*, 205422.
- (15) He, K.; Kumar, N.; Zhao, L.; Wang, Z.; Mak, K. F.; Zhao, H.; Shan, J. *Physical Review Letters* **2014**, *113*, 026803.
- (16) Mak, K. F.; He, K.; Lee, C.; Lee, G. H.; Hone, J.; Heinz, T. F.; Shan, J. *Nature Materials* **2013**, *12*, 207–211.
- (17) Xiao, D.; Liu, G.-B.; Feng, W.; Xu, X.; Yao, W. *Physical Review Letters* **2012**, *108*, 196802.
- (18) Jones, A. M.; Yu, H.; Ghimire, N. J.; Wu, S.; Aivazian, G.; Ross, J. S.; Zhao, B.; Yan, J.; Mandrus, D. G.; Xiao, D.; Yao, W.; Xu, X. *Nature Nanotechnology* **2013**, *8*, 634–638.
- (19) Plechinger, G.; Nagler, P.; Kraus, J.; Paradiso, N.; Strunk, C.; Schüller, C.; Korn, T. *Physica Status Solidi (RRL)-Rapid Research Letters* **2015**, *9*, 457–461.
- (20) Wang, G.; Marie, X.; Gerber, I.; Amand, T.; Lagarde, D.; Bouet, L.; Vidal, M.; Balocchi, A.; Urbaszek, B. *Physical Review Letters* **2015**, *114*, 097403.
- (21) Srivastava, A.; Sidler, M.; Allain, A. V.; Lembke, D. S.; Kis, A.; Imamoglu, A. *Nature Physics* **2015**, *11*, 141–147.
- (22) Zhu, Z. Y.; Cheng, Y. C.; Schwingenschlögl, U. *Physical Review B* **2011**, *84*, 153402.
- (23) Zhan, Y.; Liu, Z.; Najmaei, S.; Ajayan, P. M.; Lou, J. *Small* **2012**, *8*, 966–971.

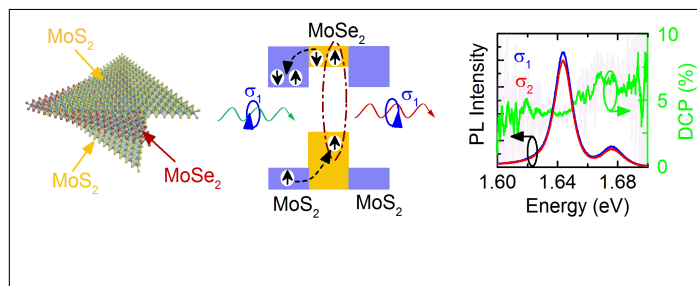
- (24) Dumcenco, D.; Ovchinnikov, D.; Marinov, K.; Lazic, P.; Gibertini, M.; Marzari, N.; Sanchez, O. L.; Kung, Y.-C.; Krasnozhon, D.; Chen, M.-W.; Bertolazzi, S.; Gillet, P.; Fontcuberta i Morral, A.; Radenovic, A.; Kis, A. *ACS Nano* **2015**, *9*, 4611–4620.
- (25) Wang, X.; Gong, Y.; Shi, G.; Chow, W. L.; Keyshar, K.; Ye, G.; Vajtai, R.; Lou, J.; Liu, Z.; Ringe, E.; Tay, B. K.; Ajayan, P. M. *ACS Nano* **2014**, *8*, 5125–5131.
- (26) Zhang, Y.; Zhang, Y.; Ji, Q.; Ju, J.; Yuan, H.; Shi, J.; Gao, T.; Ma, D.; Liu, M.; Chen, Y.; Song, X.; Hwang, H. Y.; Liu, Z. *ACS Nano* **2013**, *7*, 8963–8971.
- (27) Huang, J.-K.; Pu, J.; Hsu, C.-L.; Chiu, M.-H.; Juang, Z.-Y.; Chang, Y.-H.; Chang, W.-H.; Iwasa, Y.; Takenobu, T.; Li, L.-J. *ACS Nano* **2013**, *8*, 923–930.
- (28) Chang, Y.-H. et al. *ACS Nano* **2014**, *8*, 8582–8590.
- (29) Han, H.-V.; Lu, A.-Y.; Lu, L.-S.; Huang, J.-K.; Li, H.; Hsu, C.-L.; Lin, Y.-C.; Chiu, M.-H.; Suenaga, K.; Chu, C.-W.; Kuo, H.-C.; Chang, W.-H.; Li, L.-J.; Shi, Y. *ACS Nano* **2016**, *10*, 1454–1461.
- (30) Li, X.; Puzetky, A. A.; Sang, X.; KC, S.; Tian, M.; Ceballos, F.; Mahjouri-Samani, M.; Wang, K.; Unocic, R. R.; Zhao, H.; Duscher, G.; Cooper, V. R.; Rouleau, C. M.; Geohegan, D. B.; Xiao, K. *Advanced Functional Materials* **2017**, *27*, 1603850.
- (31) Chiu, M.-H.; Li, M.-Y.; Zhang, W.; Hsu, W.-T.; Chang, W.-H.; Terrones, M.; Terrones, H.; Li, L.-J. *ACS Nano* **2014**, *8*, 9649–9656.
- (32) Wang, K.; Huang, B.; Tian, M.; Ceballos, F.; Lin, M.-W.; Mahjouri-Samani, M.; Boulesbaa, A.; Puzetky, A. A.; Rouleau, C. M.; Yoon, M.; Zhao, H.; Xiao, K.; Duscher, G.; Geohegan, D. B. *ACS Nano* **2016**, *10*, 6612–6622.
- (33) Tongay, S.; Fan, W.; Kang, J.; Park, J.; Koldemir, U.; Suh, J.; Narang, D. S.; Liu, K.; Ji, J.; Li, J.; Sinclair, R.; Wu, J. *Nano Letters* **2014**, *14*, 3185–3190.

- (34) Mitioglu, A.; Galkowski, K.; Surrente, A.; Klopotoski, L.; Dumcenco, D.; Kis, A.; Maude, D.; Plochocka, P. *Physical Review B* **2016**, *93*, 165412.
- (35) Kang, J.; Tongay, S.; Zhou, J.; Li, J.; Wu, J. *Applied Physics Letters* **2013**, *102*, 012111.
- (36) Hong, X.; Kim, J.; Shi, S.-F.; Zhang, Y.; Jin, C.; Sun, Y.; Tongay, S.; Wu, J.; Zhang, Y.; Wang, F. *Nature Nanotechnology* **2014**, *9*, 682–686.
- (37) Ceballos, F.; Bellus, M. Z.; Chiu, H.-Y.; Zhao, H. *ACS Nano* **2014**, *8*, 12717–12724.
- (38) Wang, G.; Palleau, E.; Amand, T.; Tongay, S.; Marie, X.; Urbaszek, B. *Applied Physics Letters* **2015**, *106*, 112101.
- (39) Kioseoglou, G.; Hanbicki, A. T.; Currie, M.; Friedman, A. L.; Jonker, B. T. *Scientific Reports* **2016**, *6*, 25041.
- (40) Baranowski, M.; Surrente, A.; Maude, D.; Ballottin, M.; Mitioglu, A.; Christianen, P.; Dumcenco, D.; Kung, Y.-C.; Kis, A.; Plochocka, P. *2D Materials* **2017**, *4*, 025016.
- (41) Tongay, S.; Suh, J.; Ataca, C.; Fan, W.; Luce, A.; Kang, J. S.; Liu, J.; Ko, C.; Raghunathan, R.; Zhou, J.; Ogletree, F.; Li, J.; Grossman, J. C.; Wu, J. *Scientific Reports* **2013**, *3*, 2657.
- (42) Rigosi, A. F.; Hill, H. M.; Li, Y.; Chernikov, A.; Heinz, T. F. *Nano Letters* **2015**, *15*, 5033–5038.
- (43) Ramasubramaniam, A. *Physical Review B* **2012**, *86*, 115409.
- (44) Withers, F. et al. *Nano Letters* **2015**, *15*, 8223–8228.
- (45) Dumcenco, D.; Ovchinnikov, D.; Marinov, K.; Kis, A. High-quality synthetic 2D transition metal dichalcogenide semiconductors. 2016 46th European Solid-State Device Research Conference (ESSDERC). 2016; pp 284–286.

- (46) Ross, J. S.; Wu, S.; Yu, H.; Ghimire, N. J.; Jones, A. M.; Aivazian, G.; Yan, J.; Mandrus, D. G.; Xiao, D.; Yao, W.; Xu, X. *Nature Communications* **2013**, *4*, 1474.
- (47) Arora, A.; Nogajewski, K.; Molas, M.; Koperski, M.; Potemski, M. *Nanoscale* **2015**, *7*, 20769–20775.
- (48) Yu, Y.; Hu, S.; Su, L.; Huang, L.; Liu, Y.; Jin, Z.; Purezky, A. A.; Geohegan, D. B.; Kim, K. W.; Zhang, Y.; Cao, L. *Nano Letters* **2015**, *15*, 486–491.
- (49) Tongay, S.; Zhou, J.; Ataca, C.; Lo, K.; Matthews, T. S.; Li, J.; Grossman, J. C.; Wu, J. *Nano Letters* **2012**, *12*, 5576–5580.
- (50) Tonndorf, P.; Schmidt, R.; Böttger, P.; Zhang, X.; Börner, J.; Liebig, A.; Albrecht, M.; Kloc, C.; Gordan, O.; Zahn, D. R.; Michaelis de Vasconcellos, S.; Bratschitsch, R. *Optics Express* **2013**, *21*, 4908–4916.
- (51) Cadiz, F.; Tricard, S.; Gay, M.; Lagarde, D.; Wang, G.; Robert, C.; Renucci, P.; Urbaszek, B.; Marie, X. *Applied Physics Letters* **2016**, *108*, 251106.
- (52) Noh, J.-Y.; Kim, H.; Kim, Y.-S. *Physical Review B* **2014**, *89*, 205417.
- (53) Komsa, H.-P.; Krasheninnikov, A. V. *Physical Review B* **2015**, *91*, 125304.
- (54) Kozawa, D.; Kumar, R.; Carvalho, A.; Amara, K. K.; Zhao, W.; Wang, S.; Toh, M.; Ribeiro, R. M.; Neto, A. C.; Matsuda, K.; Eda, G. *Nature Communications* **2014**, *5*, 4543.
- (55) Kozawa, D.; Carvalho, A.; Verzhbitskiy, I.; Giustiniano, F.; Miyauchi, Y.; Mouri, S.; Castro Neto, A.; Matsuda, K.; Eda, G. *Nano Letters* **2016**, *16*, 4087–4093.
- (56) Onga, M.; Zhang, Y.; Suzuki, R.; Iwasa, Y. *Applied Physics Letters* **2016**, *108*, 073107.
- (57) Rivera, P.; Seyler, K. L.; Yu, H.; Schaibley, J. R.; Yan, J.; Mandrus, D. G.; Yao, W.; Xu, X. *Science* **2016**, *351*, 688–691.

- (58) Mai, C.; Barrette, A.; Yu, Y.; Semenov, Y. G.; Kim, K. W.; Cao, L.; Gundogdu, K. *Nano Letters* **2013**, *14*, 202–206.
- (59) Yu, T.; Wu, M. *Physical Review B* **2014**, *89*, 205303.
- (60) Dovesi, R.; Saunders, V. R.; Roetti, R.; Orlando, R.; Zicovich-Wilson, C. M.; Pascale, F.; Civalleri, B.; Doll, K.; Harrison, N. M.; Bush, I. J.; D’Arco, P.; Llunell, M. *CRYSTAL09 User’s Manual*. University of Torino. 2009.
- (61) Peintinger, M. F.; Oliveira, D. V.; Bredow, T. *Journal of Computational Chemistry* **2013**, *34*, 451–459.
- (62) Lichanot, A.; Apra, E.; Dovesi, R. *Physica Status Solidi (B)* **1993**, *177*, 157–163.
- (63) Cora, F.; Patel, A.; Harrison, N. M.; Roetti, C.; Richard A. Catlow, C. *Journal of Material Chemistry* **1997**, *7*, 959–967.
- (64) Perdew, J. P.; Burke, K.; Ernzerhof, M. *Physical Review Letters* **1996**, *77*, 3865–3868.
- (65) Grimme, S. *Journal of Computational Chemistry* **2006**, *27*, 1787–1799.

Graphical TOC Entry



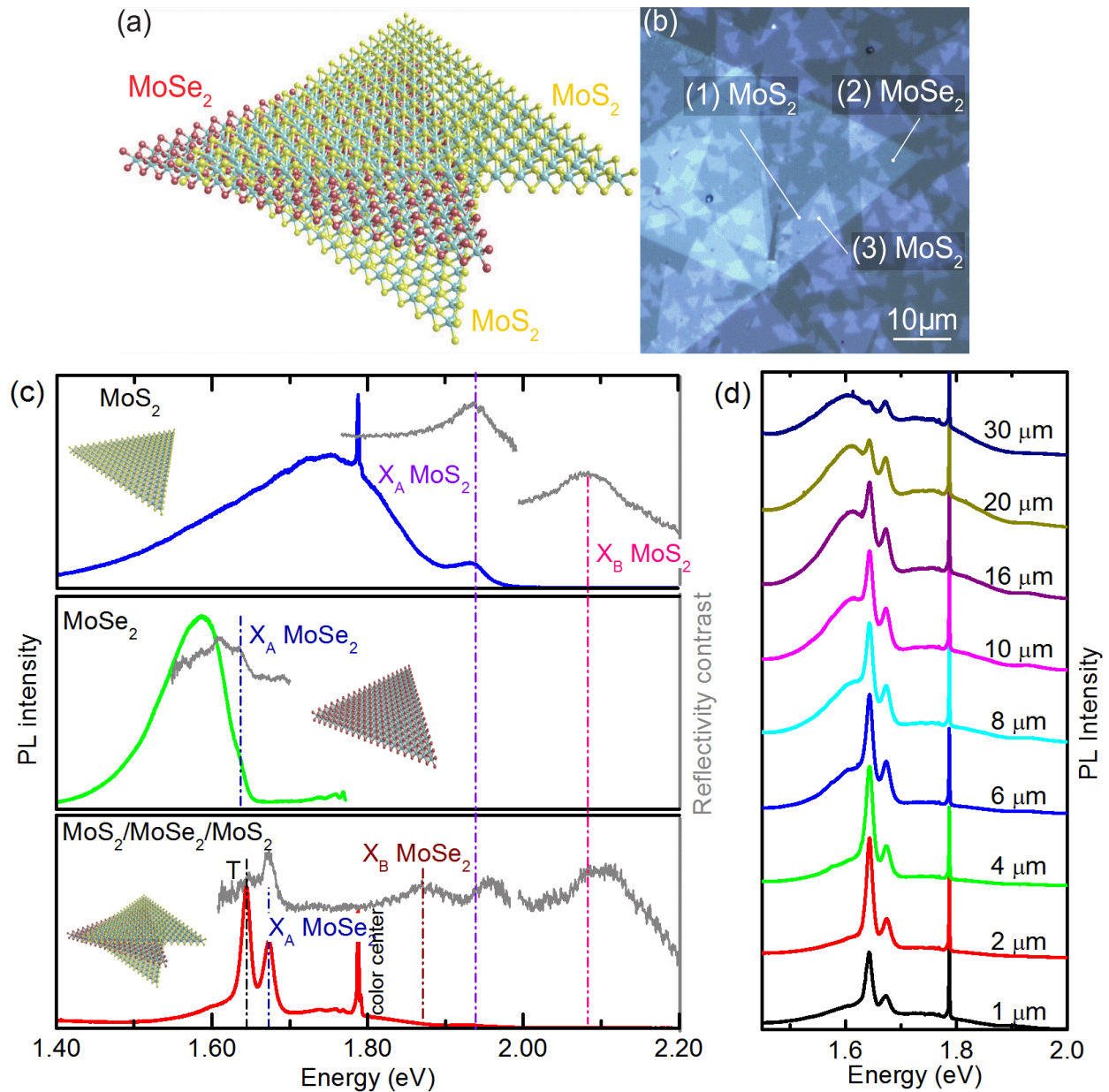


Figure 1: (a) Ball and stick model of MoSe₂ layer sandwiched between two MoS₂ flakes. (b) Optical micrograph of a representative transfer area. (c) Low temperature μ PL spectra (colored curves) and reflectivity contrast (grey curves) of as-grown MoS₂, MoSe₂ monolayers and MoS₂/MoSe₂/MoS₂ trilayer stack. (d) PL spectra of trilayer stack measured using different spot sizes. The spectra are vertically offset for clarity. X_A indicates A exciton and T denotes the trion (charged A exciton).

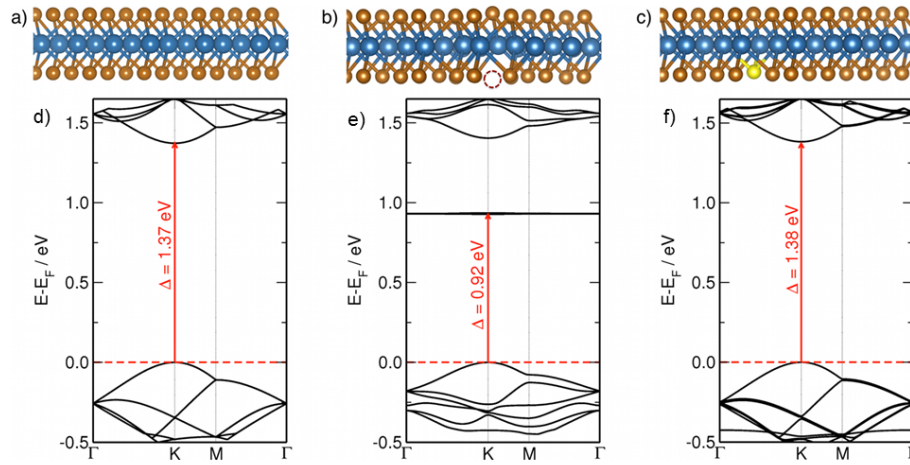


Figure 2: (a)–(c) Atomic representation of a perfect MoSe₂ monolayer, the MoSe₂ monolayer with 1 Se vacancy, and the MoSe₂ monolayer with 1 S substitution, respectively. (d)–(f) Calculated corresponding band structures. Fermi level (horizontal dashed lines) is shifted to the top of the valence band. Fundamental bandgaps are indicated.

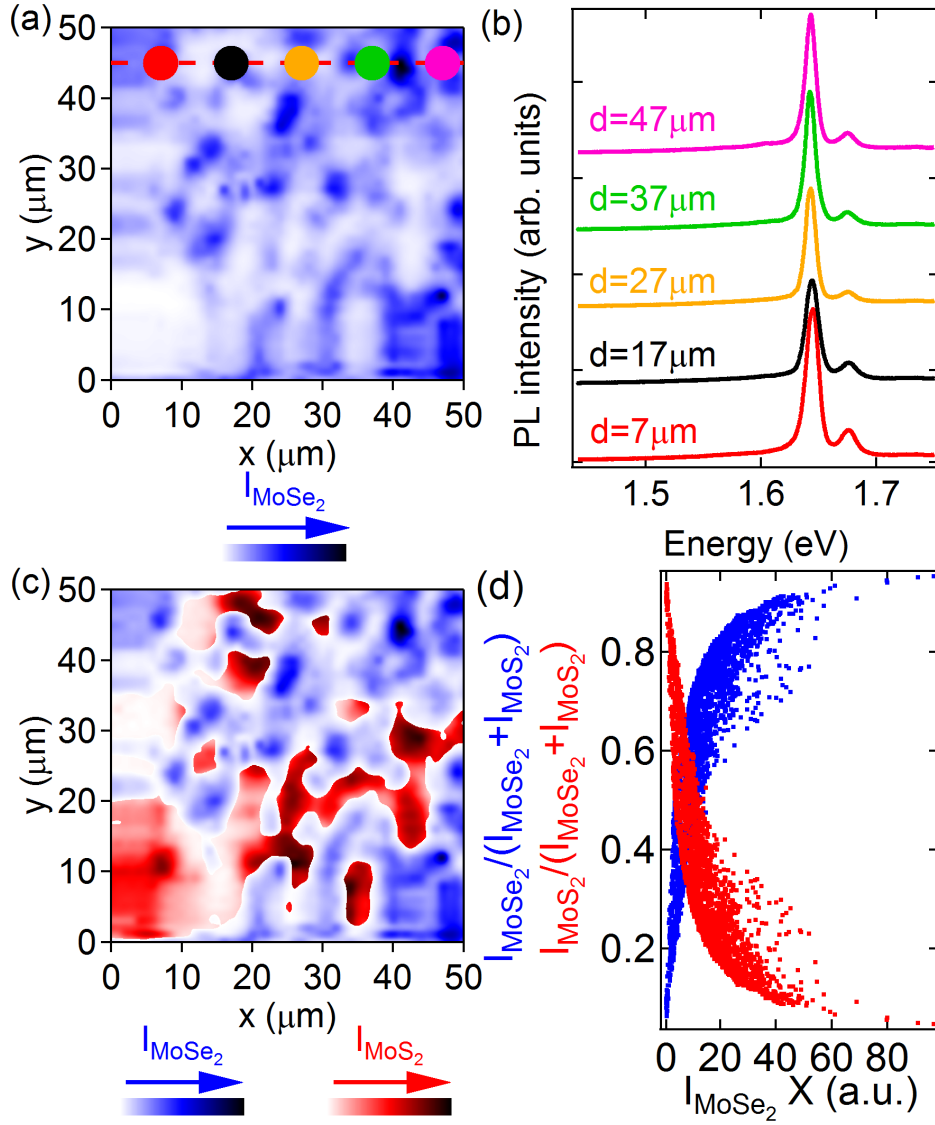


Figure 3: (a) Spatial map of the integrated intensity of A exciton of encapsulated MoSe₂. The dashed line schematically illustrates the direction along which the spectra of panel (b) have been extracted. The colored circles mark the position within the map of the spectra having the corresponding color in panel (b). (b) μ PL spectra extracted at positions marked by circles of the corresponding color in panel (a). The spectra are vertically offset for clarity. (c) Mapping of the integrated intensity of MoS₂ X_A overlaid on the same spatial map of MoSe₂ X_A. (d) Integrated intensity of MoSe₂ X_A and MoS₂ X_A as a function of the intensity of MoSe₂ X_A.

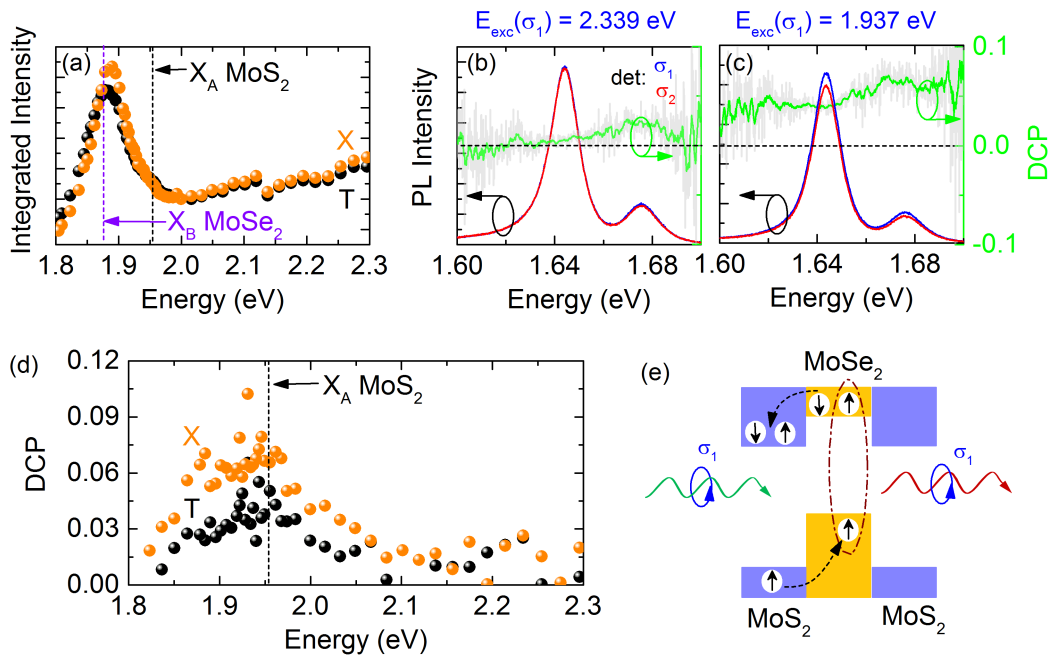


Figure 4: (a) Normalized integrated intensity of MoSe₂ X_A as a function of the excitation energy. Polarization resolved μPL spectra and DCP of MoSe₂ excited (b) far off MoS₂ X_A resonance and (c) on resonance with MoS₂ X_A. (d) Integrated DCP as a function of the excitation energy. (e) Schematic illustration of spin transfer under excitation resonant with MoS₂ X_A.